Piezoelectricity and Related Properties in Orthorhombic Cadmium Diiodate

H. Azeroual, J.-L. Bantignies, L. Alvarez, D. Maurin, D. Granier, J. Haines, O. Cambon, P. Hermet

Journal Name

Piezoelectricity and Related Properties in Orthorhombic Cadmium Diiodate[†]

H. Azeroual,[a] J.-L. Bantignies,[b] L. Alvarez,[b] D. Maurin,[b] D. Granier,[a] J. Haines,[a] O. Cambon,[a] and P. Hermet[a‡]

We report a complete investigation of the structural, electronic, vibrational, elastic and piezoelectric properties of the $P2_12_12_1$ orthorhombic phase in cadmium diiodate (δ-Cd(IO$_3$)$_2$) by combining experiments and first-principles based calculations. We revisited the nature of the electronic band gap and suggest an indirect band gap with a value of 4.6 eV. The infrared and Raman responses were measured and the different phonon modes assigned. To date, the δ-Cd(IO$_3$)$_2$ piezoelectric response remains unknown. We reported the different mechanisms involved in its piezoelectric response from the density functional perturbation theory. The highest value of the piezoelectric-stress and piezoelectric-strain constants in the zero Kelvin limit is predicted for e_{41} =-0.27 C/m^2 and d_{41} =-10.32 pC/N. These sizable values associated with the thermal stability (no phase transition up to the thermal decomposition at 550 °C) and a relative large electronic band gap make δ-Cd(IO$_3$)$_2$ a potential candidate for piezoelectric applications.

1 Introduction

Non centro-symmetric metal iodates with a lone-pair located on the I(V) atom are very attractive materials for second harmonic generation (SHG) applications with wide transparency wavelength regions (up to 12 μm), large SHG coefficients[1] (up to 400 times higher than α-SiO$_2$ for La(IO$_3$)$_3$) and high optical-damage thresholds[1–9] (up to 50 GW.cm^{-2}). Sun *et al.*[10] published in 2011 a review on the structure–property relationships of metal iodates. They pointed out that the presence of both types of asymmetric units issued from d^0 transition-metal cations (with the second order Jahn-Teller distortion) and iodate anions (due to the lone-pair) induces additional effects hence promoting the polarizability of the material, and finally increasing the SHG properties. Numerous formulae of iodates (M^{I}IO$_3$, M^{II}(IO$_3$)$_2$, M^{III}(IO$_3$)$_3$)[11–17] and mixed iodates (M^{I}M^{II}(IO$_3$)$_3$, M^{II}M^{II}(IO$_3$)$_4$, M(IO$_3$)X)[18–20] have been already studied. Nevertheless, this principle of acentricity, through non-bonded electrons, is today little explored for piezoelectric applications.

Here, we focus on the iodates of the M^{II}(IO$_3$)$_2$-type materials and more especially on the $P2_12_12_1$ orthorhombic phase of cadmium diiodate (δ-Cd(IO$_3$)$_2$, labelled CDI in the following). This phase was selected because it brings together: acentricity, no twin and large thermal stability among the M^{II}(IO$_3$)$_2$ family[17,21], which are some requirements for considering a potential piezoelectric material. Theoretically, CDI has never been investigated by a first-principles based method or other types of calculation. Experimentally, some articles have been reported in the literature. Nevertheless, these studies are rather restricted on the structural characterization and the SHG measurements. In 1976, Bach grew CDI single crystals with a size of several millimeters[22] and determined the crystallographic structure[23]. Ravi Kumar *et al.*[24] grew bulk size single crystals (11×10×2 mm^3) by using slow-cooling method for SHG applications. SHG and electronic properties have also been investigated by Ravi Kumar *et al.*[24]. However, their observations on SHG are not consistent with the measurements of Shitole[25]. Ravi Kumar *et al.*[24] measured a SHG efficiency higher in CDI than in potassium dihydrogen phosphate (KDP) whereas Shitole[25] observed the opposite trend. This inconsistancy could be related to the crystal quality. In contrast to SHG, the experimental vibrational dynamics of CDI have been almost unexplored. Only the mid-infrared spectrum has been reported with an attempt to assign the iodate groups[25]. The piezoelectric properties remain still unknown today.

In this article, we report a complete investigation of the structural, electronic, vibrational, elastic and piezoelectric properties in CDI. This study covers the synthesis and the analysis of physical characterizations by combining experiments and first-principles based calculations. We synthetized and characterized a CDI single crystal. A complex polymorphism in terms of synthesis conditions have been reported[21,26]. We revisited the nature of the electronic bandgap of this compound using UV-vis spectroscopy and calcu-

[a] ICGM, Univ. Montpellier, CNRS, ENSCM, Montpellier, France
[b] Laboratoire Charles Coulomb (L2C), CNRS, University of Montpellier, France
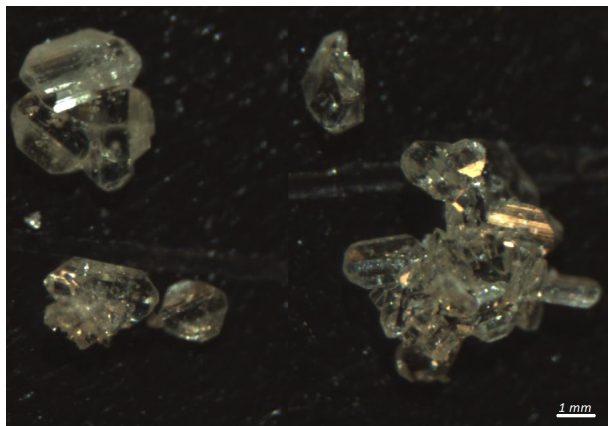‡ Corresponding author. E-mail: patrick.hermet@umontpellier.fr

Fig. 1 Single crystals of CDI.

lations of the electronic band structure. The vibrational properties were measured by infrared and Raman spectroscopies. The different phonon modes were assigned using density functional perturbation theory by direct comparison with the experiments. We predicted the different piezoelectric tensors and reported the mechanisms involved in the CDI piezoelectric response. This part is purely theoretical as piezoelectric measurements were not possible due to the small size of our single crystals. In this context, the calculated piezoelectric constants were decomposed into an electronic and a phonon-mediated contribution. The latter contribution was also analyzed using two complementary approaches: the normal modes of vibration and the different polyhedra used as building block of the CDI structure. This method of calculation succeeded in the prediction and the understanding of α-quartz-type piezoelectric compounds [27–30]. The CDI dielectric constants were also analyzed as a function of the electronic, vibrational and piezoelectric contributions.

2 Synthesis and Experimental setup

2.1 Synthesis and crystal growth

The used synthesis method was that developed by Ravi Kumar *et al.* [24]. The first step is the synthesis of the γ-Cd(IO$_3$)$_2$ phase by using 1.42×10^{-3} moles of CdCl$_2$ (99 %) and 2.84×10^{-3} moles of HIO$_3$ (99.5 %) from Sigma Aldrich in a stoichiometric ratio of 1:2 according to the following reaction: $CdCl_2 + 2HIO_3 \longrightarrow Cd(IO_3)_2 + 2HCl$. The two reactants were dissolved in water, mixed and stirred for 4 hours at ambient temperature (20°C). The white precipitate, γ-Cd(IO$_3$)$_2$, was collected and dried in an oven at 100°C. Going through the phase γ is the only way to get to the pure δ-phase without the other four polymorphs (α, β, ε and ζ) [21]. Then, 0.26 g of the γ-Cd(IO$_3$)$_2$ compound was dissolved in 30 ml of HNO$_3$ (9.5 mol/L) in an airtight beaker using a magnetic stirrer maintained at constant temperature (60°C). After attaining saturation (pH=2), the beaker was kept in a thermostatic bath maintaining the temperature stable. After 5 days, optically transparent and defect-free tiny crystals are obtained by self-nucleation by slow evaporation (Figure 1).

2.2 Single crystal X-ray diffraction and thermal analyses

Suitable CDI single crystals ($60 \times 120 \times 140 \ \mu$m) were mounted on a cryoloop and crystal structures were determined by x-ray diffraction using a Bruker 4-circle D8 Venture diffractometer with a PHOTON II area detector, using Mo K$_\alpha$ radiation (0.71073 Å) from an incoated IμS 3.0 microsource with focusing mirrors operating at 50 kV and 1 mA. The data collection was performed at 298 K and the structures were solved by direct methods using SHELXS 2013/1 software and refined by full-matrix least-squares using SHELXL 2014/7 software. The absorption correction type is multi-scan performed by SADABS-2016/2 - Bruker AXS area detector scaling.

The thermogravimetric analysis was carried out on crushed CDI single crystals by using a NETZSCH STA 449F1 analyzer with an heating rate of 2°C/min under an Ar flow in the temperature range from 20 to 1200°C.

2.3 Spectroscopic techniques

Mid- and far-infrared measurements, respectively in the 450–4000 and 40–650 cm^{-1} range, were carried out on a Bruker IFS 66V Fourier transform spectrometer using a black body source. A series of two different beamsplitters covered the whole spectral region: KBr (mid-infrared) and Ge-coated (far-infrared). A Si-bolometer detector cooled at 4 K and a N$_2$-cooled MCT (mercury cadmium telluride) detector were respectively used to probe the far- and mid-infrared domains with extra sensitivity. The spectral resolution was 2 cm^{-1} and 64 scans were accumulated for each spectrum. The measurements were performed in the 35–295 K range using a cold finger helium cryostat. The CDI sample was gently ground with polyethylene powder (6.4% in concentration) in the far-infrared or with bromide potassium powder (0.3% in concentration) in the mid-infrared and compressed under 8 tons to form an isotropic pellet of 12 mm diameter.

Raman experiments were performed at room temperature on a T64000 spectrometer from Horiba-Jobin-Yvon using a triple monochromator configuration. We worked in backscattering geometry and we used the 491 nm line from a COBOLT laser diode. The beam was focused using a 50x lens. Different laser powers were tested to get rid from the heating of the sample and a power of 7 mW was chosen. The spectral resolution was 2 cm^{-1}.

The UV-vis spectrum was recorded in transmittance mode using a VARIAN Cary 5000 spectrometer at room temperature. The CDI compound was placed in suspension in water. Data were collected within the 200–1200 nm range with a resolution and an integration time of 1 nm and 0.3 s, respectively.

3 Computational details

The zone-center dynamical matrix, Born effective charges, dielectric, elastic and piezoelectric tensors have been calculated within a variational approach to density functional perturbation theory as implemented in the ABINIT package [31]. The exchange-correlation energy functional is evaluated using the generalized gradient approximation (GGA) parametrized by Perdew, Burke and Ernzerhof (PBE) [32]. A Van der Waals semi-empirical dispersion potential with Becke-Jonhson damping [33] and refined

by Grimme *et al.* [34] was also included as correction to the PBE exchange-correlation energy (DFT-D3). This model will be called PBEvdW in the following. The all-electron potentials are replaced by norm-conserving pseudopotentials generated according to the Troullier-Martins scheme. $Cd(4s^2, 4p^6, 4d^{10}, 5s^2)$, $I(5s^2, 5p^5)$ and $O(2s^2, 2p^4)$-electrons are considered as valence states. Athough iodine is a heavy element, the spin-orbit coupling has been neglected in our calculation. The electronic wave functions are expanded in plane-waves up to a kinetic energy cutoff of 67 Ha and integrals over the Brillouin zone are approximated by sums over a $8\times4\times8$ mesh of special k-points according to the Monkhorst-Pack scheme [35]. These k-point sampling and kinetic energy cutoff give converged results. Lattice parameters and atomic positions were fully relaxed using a Broyden-Fletcher-Goldfarb-Shanno algorithm until the maximum stresses and residual forces were less than 7×10^{-4} GPa and 6×10^{-6} Ha/Bohr, respectively. Electronic density of states (DOS) have been calculated using a Γ-centered $16\times16\times16$ k-point grid (512 points in the IBZ) at the PBE and PBEvdW levels. DOS calculations using meta-GGA functionals have been performed with the projector augmented wave method and an energy cutoff of 500 eV as implemented in VASP [36]. In our calculations, our (x, y, z) orthogonal reference system is collinear to the (a, b, c) crystal system.

4 Results and discussion

4.1 Crystallographic structure

Our crystallographic characterization on a single crystal shows that CDI crystallizes at room temperature in the acentric orthorhombic $P2_12_12_1$ (D_2^4) space group with four formula units (Z=4) per unit cell and the cell parameters: $a =5.856(10)$, $b =17.480(3)$ and $c =5.588(10)$ Å. The asymmetric unit contains one cadmium, two iodine and six oxygen atoms. All atoms occupy the general $4a$ Wyckoff position. Data collection and refinement details are listed in Tables S1† (ESI). The CIF file has been deposited at the Cambridge crystallographic data centre with deposition number: ICSD 2144368. Our refined structure is in excellent agreement with the structure reported by Bach *et al.* [23] as indicated by the very small values of the lattice distortion ($\eta =0.04\%$) and the similarity factor [37] ($\Delta =0.5\%$) [38].

The thermogravimetric analysis (TGA) shows that the CDI compound is stable until 550°C (Figure 2). From this temperature, we observe a mass loss of 72.5% consistent with the theoretical mass loss of 72.2% when $Cd(IO_3)_2$ transforms to CdO. The thermal decomposition after 550°C can therefore be written as follows: $Cd(IO_3)_2 \longrightarrow CdO(s) + I_2(g) + \frac{5}{2}O_2(g)$. Shitole demonstrated a progressive decomposition of $Cd(IO_3)_2$ by I_2 and O_2 release with $Cd_5(IO_4)_2$ as the final compound [25]. In our case, CdO is clearly identified by x-ray diffraction consistent with the mass loss (inset in Figure 2). By cooling under air, CdO partially transforms into $Cd(OH)_2$ with atmospheric water. The TGA published by Ravi Kumar *et al.* [24] presents a mass loss at 380°C which is attributed to the δ-ε phase transition of cadmium diiodate. From our point of view, this mass loss has rather to be attributed to a water impurity content released from the crystal during heating.

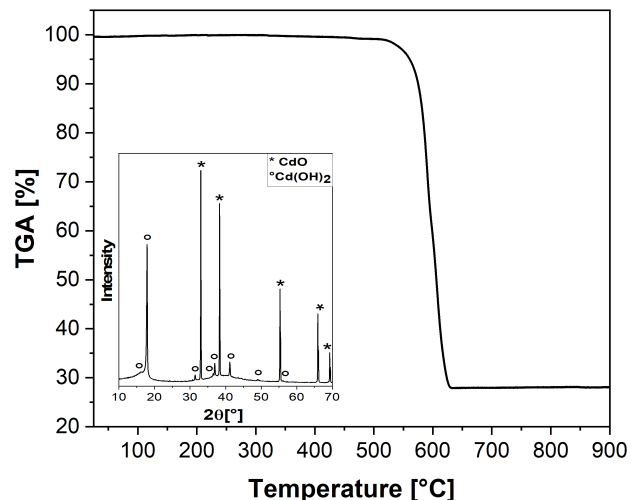Considering a polyhedral representation, the CDI structure can

Fig. 2 Thermogravimetric analysis (TGA) for CDI. Inset: x-ray diffraction data of the final decomposition obtained after TGA.

be seen as a distorted corner-sharing CdO_7 pentagonal bipyramids connected via oxygen-atoms (by edge or corner) to two IO_3^- trigonal pyramids (Figure 3). The geometry of these trigonal pyramids are attributed to the I $5s^2$ lone-pair. All the CdO_7 polyhedra are equivalent in the structure whereas two IO_3^- polyhedra are inequivalent. They have been displayed in different colours in Figure 3. The iodate polyhedra in yellow (labelled P(I1)) are connected to two CdO_7 polyhedra whereas the grey polyhedra (termed P(I2)) are connected to three CdO_7 polyhedra. The Cd-O bond lengths range from 2.27 to 2.50 Å. The I-atoms are strongly bonded to the three oxygens of the iodate group at distances between 1.81 and 1.83 Å and weakly bonded to three further oxygens at longer distances between 2.58 and 2.77 Å.

This experimental CDI structure has been considered as input in our DFT-based structural relaxations. To evaluate the influence of the exchange–correlation functional on the CDI structure, two other functionals have been considered in addition to the PBE. The first also belongs to the GGA class and is a reformulation of PBE especially adapted for solids (PBEsol) [39]. The second is the Perdew-Wang parameterization (PW) [40] and belongs to the functional class of the local density approximation (LDA). Influence of the empirical van der Waals correction to the PBE exchange-correlation energy has also been studied. All results are listed in Table 1. The calculation using the PBE functional shows an overestimation of the lattice parameters in the three directions (up to +2.1% for the c-lattice parameter), leading to an overestimation of +3.7% of the experimental unit cell volume. In contrast, the three lattice parameters are underestimated with the PBEsol functional. This underestimation reaches -2.4% for the b lattice parameter and -4.6% for the volume. The same trend is observed with the Perdew-Wang (PW) functional at the LDA level with a more severe underestimation going up to -4.5% for the b lattice parameter and -10.1% for the unit cell volume. The PBE func-

	Expmt.	PBE (GGA)	PBEvdW (GGA)	PBEsol (GGA)	PW (LDA)
Lattice parameters					
a (Å)	5.856(10)	5.914 (+1.0)	5.814 (-0.7)	5.761 (-1.6)	5.654 (-3.4)
b (Å)	17.480(3)	17.580 (+0.6)	17.235 (-1.4)	17.067 (-2.4)	16.701 (-4.5)
c (Å)	5.588(10)	5.703 (+2.1)	5.609 (+0.4)	5.552 (-0.6)	5.445 (-2.6)
Ω_0 (Å^3)	572.00(17)	592.93 (+3.7)	562.05 (-1.7)	545.87 (-4.6)	514.16 (-10.1)
Intrapolyhedral distances (Å)					
$<d(Cd\text{-}O)>$	2.379(2)	2.407 (+1.2)	2.378 (+0.0)	2.354 (-1.0)	2.315 (-2.7)
$<d(I1\text{-}O)>$	1.823(2)	1.875 (+2.9)	1.880 (+3.1)	1.872 (+2.7)	1.878 (+3.0)
$<d(I2\text{-}O)>$	1.828(2)	1.886 (+3.2)	1.894 (+3.6)	1.887 (+3.2)	1.897 (+3.8)
Intrapolyhedral distortions (%)					
$\delta[P(Cd)]$	2.46	2.30	2.30	2.16	2.23
$\delta[P(I1)]$	0.39	0.44	0.73	0.72	1.13
$\delta[P(I2)]$	0.12	0.30	0.57	0.77	1.28
Intrapolyhedral volumes (Å^3)					
$\Omega[P(Cd)]$	19.90	20.67	19.92	19.32	18.36
$\Omega[P(I1)]$	0.98	1.07	1.09	1.07	1.09
$\Omega[P(I2)]$	1.00	1.10	1.12	1.11	1.14
Interpolyhedral distances (Å)					
Cd-Cd	4.395(1)	4.439 (+1.0)	4.355 (+0.9)	4.323 (-1.6)	4.225 (-3.9)
Cd-I1	3.243(1)	3.305 (+1.9)	3.293 (+1.5)	3.276 (+1.0)	3.264 (+0.6)
Cd-I2	3.280(1)	3.337 (+1.7)	3.321 (+1.3)	3.300 (+0.6)	3.286 (+0.2)
I1-I2	3.603(1)	3.601 (+0.1)	3.532 (-2.0)	3.491 (-3.1)	3.434 (-4.7)

Table 1 Selected structural parameters in CDI calculated at 0 K for different exchange–correlation functionals (see text) and compared to experiment at 295 K. Relative errors with respect to the experimental values (in %) are given between brackets for the different functionals.
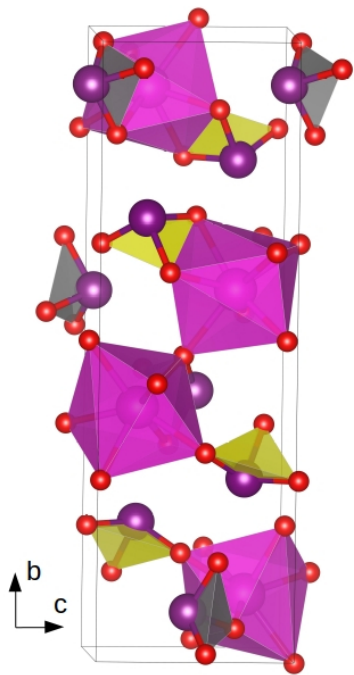
Fig. 3 Crystal structure of CDI viewed along the a-axis highligthing the three different polyhedra. The polyhedra centered on Cd-, I1- and I2-atoms are displayed in pink, yellow and grey, respectively.

tional therefore shows the best agreement with the experimental lattice parameters. The consideration of a van der Waals-type correction to the PBE exhange-correlation energy (PBEvdW) gives a systematic decrease of the calculated PBE lattice parameters (Table 1) and improves the agreement with the experimental lattice parameters as the overall absolute relative error is below 1.4%. The unit cell volume is also better predicted with PBEvdW.

For the atomic distances, each model has been evaluated according to three main characteristics on polyhedra (Table 1): the mean distance ($<d>$) between the central atom and the coordinating oxygens, the volume (Ω) and the distortion (δ). The latter has been calculated for each polyhedron P(X) as:

$$\delta[P(X)] = \frac{1}{N}\sum_{i=1}^{N}\frac{|d_i - <d>|}{<d>}, \qquad (1)$$

where N is the coordination number of the central atom X ($N = 7$ for $X = $ Cd and $N = 3$ for $X = $ I1 or I2) and d_i is the distance from the central atom in a polyhedron to the ith coordinating oxygen atom. We observe that the PBE and PBEvdW give similar results. Both describe quite well the CdO$_7$ polyhedra and the interpolyhedron distances. The mean distances show a maximal absolute relative error of 2% and an excellent prediction on the distortion of the CdO$_7$ polyhedra with respect to the experiment. Nevertheless, they fail to correctly describe the iodate polyhedra as we observe a relative error about +3% on mean distances. The distortion of these polyhedra is slightly higher with the van der Waals correction. The PBEsol description of the polyhedron geometries are a little worse than for PBE or PBEvdW as the distor-

tion of the polyhedra centered on I2 iodine and the I1-I2 mean distance are higher. The LDA/PW functional clearly shows the poorest agreement with the experimental data highlighting an inadequacy to reproduce the CDI structure. This functional considerably increases the distortion of the iodate polyhedra (more than threefold) which could be related to a too strong delocalization of the iodine lone-pair in the calculation.

Considering the overall structure description and the strong temperature difference between the experiment (298 K) and the calculations (0 K), we privileged the PBEvdW model for the prediction of the electronic, vibrational and piezoelectric properties in CDI.
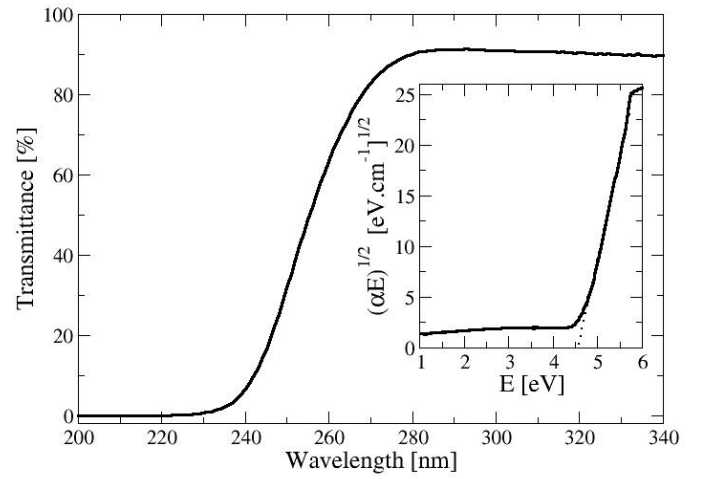
4.2 Electronic band structure

Figure 4 displays the UV–vis spectrum of CDI using a transmittance configuration. The transmission edge estimated from the inflexion point is located at about 255 nm. The band gap energy, E_g has been estimated using the Tauc's plot method[41] which is based on the assumption that the energy-dependent absorption coefficient, α, can be expressed as:

$$(\alpha E)^n \propto (E_g - E), \tag{2}$$

where E is the photon energy. The n-parameter depends on the nature of the optical transition and for allowed transitions it can only have two values: $n = 2$ for direct transition band gap and $n = 1/2$ for indirect transition. The optical band gap can be estimated from the extrapolation to zero of the linear regions in the $(\alpha E)^n$ vs E plots. The better fit between $n = 2$ or $n = 1/2$ thus identifies the correct type of electronic transition. In the case of CDI, we can observe a linear dependence both for the $(\alpha E)^{\frac{1}{2}}$-plot and the $(\alpha E)^2$-plot (see Figure S1† in ESI). Nevertheless, we found that the $(\alpha E)^{\frac{1}{2}}$-plot gives a better fit, suggesting an indirect band gap of 4.6 eV (inset of Figure 4). Our analysis does not support the work of Ravi Kumar *et al.*[24] where a direct bandgap of 3.85 eV was also determined from UV-vis and Tauc's plot method using $n = 2$.
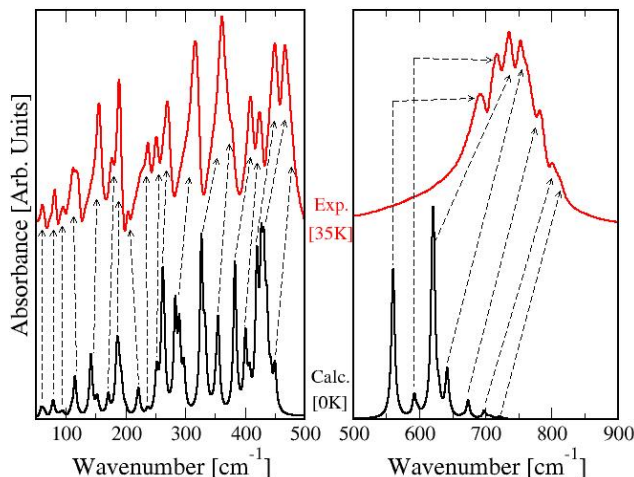
The electronic band structure calculated at the PBEvdW level along the high symmetry points in the first Brillouin zone is displayed in Figure 5. The bottom of the conduction band is at the Γ-point of the Brillouin zone. The top of the valence band is located between the Y and Γ-point, but we cannot exclude a localization at the Γ-point considering the very small dispersion of the valence band along the Y–Γ line. This is the reason why we checked that a calculation at the experimental volume or using different functionals (like PBE and PBEsol) preserves the position of the top of the valence band between the Y and Γ-point. Projected density-of-states show that the conduction band is mainly composed of hybridized I 5p and O 2p orbitals. The valence band is dominated by O 2p orbitals with small contributions of the Cd 4d and I 5p orbitals. The calculated energy bandgap, $E_g = 2.85$ eV at the PBEvdW level, is much smaller than our experimental band gap energy (or that of Ravi Kumar and coworkers) measured by UV-vis spectroscopy. This band gap problem is well known in DFT and related to the derivative discontinuity of the LDA/GGA exchange-correlation energy[42]. Thus,

Fig. 4 Experimental UV-vis spectrum of CDI in transmittance configuration. Inset: $(\alpha E)^{\frac{1}{2}}$ Tauc plot. The extrapolation of the linear part is shown in dashed line.
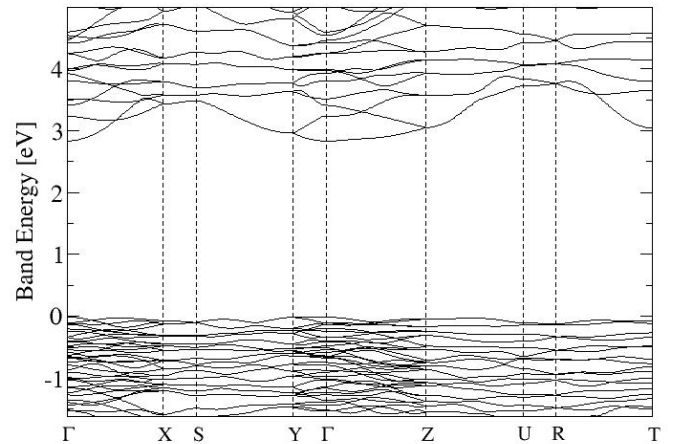
Fig. 5 Calculated electronic band structure of CDI using the PBEvdW model. The position of the Fermi energy is set to 0 eV.

Fig. 6 Experimental (35 K) and calculated (0 K) infrared absorbance spectra of CDI. The calculated spectrum is displayed using a Lorentzian line shape and a constant linewidth fixed at 2 cm^{-1}.

we also computed the electronic band structure beyond standard LDA/GGA using meta-GGA (m-GGA) functionals like the variational Strongly Constrained and Appropriately Normed (SCAN) functional[43] and the non-variational Tran-Blaha modified Becke-Jonhson (TB-mBJ) functional[44]. These m-GGA functionals have proven to be as accurate as hybrid functionals (or GW) for the band gap prediction, but with a computational cost similar with standard LDA/GGA functionals. Our two m-GGA calculations also predict an indirect band gap with a calculated value of E_g =3.5 eV (SCAN) and 4.2 eV (TB-mBJ). All our calculations (GGA and m-GGA) therefore support an indirect band gap in CDI in agreement with our UV-vis measurement. However, the value of E_g should be confirmed at the GW level as we get quite dispersive values ($E_g \sim$ 3.5–4.2 eV) between the SCAN and TB-mBJ functionals. Similarly, further experiments to explore the influence of the crystal quality on the band gap value could be required to unambiguously determine E_g.

4.3 Zone-center lattice dynamics

The CDI point group is D_2. Based on the group theory, this point group has four non-degenerate irreducible representations: A, B_1, B_2 and B_3. The nine atoms of the CDI asymmetric unit are located on C_1-site symmetry and vibration modes of each of them contribute to the following irreducible representation: $3(A \oplus B_1 \oplus B_2 \oplus B_3)$. Thus, the corresponding irreducible representation of the acoustic (Γ_{acc}) and optical (Γ_{opt}) vibrational modes at the zone-center (Γ-point) are: $\Gamma_{acc} = B_1 \oplus B_2 \oplus B_3$ and $\Gamma_{opt} = 27A \oplus 26(B_1 \oplus B_2 \oplus B_3)$. Among these optical modes, all are Raman active and only modes belonging to the B_1, B_2, or B_3 irreducible representation are infrared active. The calculated frequencies of the 105 zone-center transverse-optical modes are listed in ESI (Table S2†).

The temperature dependence of the CDI infrared responses is displayed between 35 and 295 K in Figures S2 (50–550 cm^{-1}) and S3 (500–950 cm^{-1}) (see ESI). The frequencies above 950 cm^{-1} are not shown because they do not bring additional information on the material. We observe a quasi-harmonic dependence of the phonon bands with the temperature within the 50–550 cm^{-1} range. All the bands show an usual frequency up-shift when the temperature decreases (<10 cm^{-1}) related to the strengthening of the effective force constants. In contrast, the bands within the 500–950 cm^{-1} range show a softening in frequency with decreasing temperatures (up to -7 cm^{-1} for the band about 700 cm^{-1}), different from the anharmonicity of a normal optical phonon. This redshift is associated to the presence of interatomic I...O halogen bonds in the compound. Indeed, similar to the behavior observed in an intermolecular hydrogen bond[45], a decrease in the intramolecular I-O force constants is expected when the intermolecular I...O halogen bonds are subjected to low temperature. We do not observe the appearance of new bands between 50 and 950 cm^{-1}. Thus, the existence of a phase transition in CDI driven by a polar mode is ruled out.

The experimental infrared spectrum measured using an absorbance configuration at 35 K is reported in Figure 6 within the 50-900 cm^{-1} range. The DFT infrared spectrum calculated at 0 K and using the formalism described in ref.[46] is also reported in this figure. The band width cannot be calculated within the framework of the harmonic approximation and is arbitrarily fixed at 2 cm^{-1}. Below 50 cm^{-1}, a B_2 mode calculated at 41 cm^{-1} is expected and experimentally evidenced at room temperature at 39 cm^{-1}. This mode is not observed at 35 K because the 40–50 cm^{-1} range (corresponding to the limit of the IR bandwidth) cannot be probed due to additional optical loss in the cryostat windows. The experimental spectrum can be divided into two regions. The first (50–500 cm^{-1}) shows several intense bands. The number of bands, their frequency position and their relative intensity are in acceptable agreement with the calculation. The arrows added in the figure is a help to the reader for the identification of the calculated bands to the experimental ones. The second region (500-900 cm^{-1}) is dominated by a very intense and broad experimental band with a complex multi-structure. The average position of this broad experimental feature is strongly underestimated by the calculation ($\sim$100 cm^{-1}). Nevertheless, the number of experimental band and their relative intensities are quite well calculated. This same frequency underestimation was also observed in this domain for other iodates such as α-LiIO$_3$ (PBE[47] or PBEsol[12]) and Fe(IO$_3$)$_3$ (DFT+U formalism[48]). The origin of this behavior is not presently understood but could require to go beyond (i) the standard GGA functionals in DFT or (ii) the harmonic approximation for building the dynamical matrix.

Assignment of the infrared band to a particular motion of atoms is not a trivial task without the support of DFT calculations. Nevertheless, the polyhedral configuration of CDI could simplify the process. As determined by x-ray diffraction, the CDI structure is based on a distorted CdO$_7$ pentagonal bipyramids connected to IO$_3^-$ pyramids. A free iodate ion belongs to the C_{3v} molecular point group with the irreducible representation for the internal modes: 2A$_1$+2E. These representations, both Raman and

infrared active, correspond in Herzberg's notation[49] to the six intramolecular normal modes: ν_1, ν_2, ν_3 and ν_4, where the two last modes are doubly degenerate. The $\nu_1(A_1)$ (resp. $\nu_3(E)$) vibration is a symmetric (resp. antisymmetric) stretching located in the 630–780 cm^{-1} (resp. 730–820 cm^{-1}). The $\nu_2(A_1)$ (resp. $\nu_4(E)$) vibration is a symmetric (resp. antisymmetric) deformation located in the 320–400 cm^{-1} (resp. 400–450 cm^{-1}). However, the presence of distortions induce noticeable changes in the frequency position of these modes and their degeneracies. Indeed, the low site symmetry (C_1) of the iodate groups in CDI lifts all the degeneracies of the C_{3v} molecular point group to yield to an unique non-degenerate A-representation. From a correlation procedure, we can show that each A-representation can be decomposed into $A \oplus B_1 \oplus B_2 \oplus B_3$ within the D_2 point group. As we have two crystallographic independent iodate groups, we conclude that 18 infrared modes should be active in the range of iodate stretching vibrations: 6 are symmetric stretching vibrations and 12 are antisymmetrics. Based on the analysis of the eigendisplacement vectors of each normal mode, we assigned the broad band located between 500 and 900 cm^{-1} as stretching vibrations of the iodate groups. The ν_1 (resp. ν_3) vibrations are calculated in the 690-800 (resp. 500-690) cm^{-1} range. This results contrasts with the frequency range where the ν_1 and ν_3 vibrations of a free iodate ion are observed[25,50,51] and shows the limitation of the free polyhedron model. The identification with our experimental spectrum shows that only 8 experimental bands (over the 18 expected) can be observed considering the resolution of our experimental spectrum (Figure 6). These contributions, located at (35 K) 692, 717, 736, 753, 764, 782, 803 and 813 cm^{-1} (Table 2), are consistent with the usual observed stretching modes in iodate based compounds[47,50,51]. Similarly, 18 infrared active modes (6 symmetric and 12 antisymmetric) are expected from group theory analysis within the frequency range of iodate deformations (270–500 cm^{-1}). Of these 18 modes, 11 can be observed in Figure 6 and their frequencies are listed in Table 2. From the analysis of the eigendisplacement vectors, the modes between 400 and 500 cm^{-1} are assigned to ν_4 vibrations. Those between 270 and 400 cm^{-1} are ν_2 vibrations. The modes below 270 cm^{-1} have been associated with the translational, rotational and librational motions of the iodate groups as rigid units. The calculated frequency of all infrared modes in CDI are listed in Table S2 (ESI).

Assignment of the Raman modes is more difficult than the infrared ones because A-modes are active in addition to the infrared modes previously discussed (see Figure 7). A total of twelve additional Raman A-lines (six associated to stretching and six others to deformation of iodate groups) are expected. In the region of the iodate stretching modes, three experimental A-lines could be assigned at 705 732, and 774 cm^{-1} as they do not have their counterpart in the infrared spectrum. These lines are predicted at 577, 623 and 701 cm^{-1} in our DFT calculations, respectively. Similarly, one experimental Raman A-line could be assigned at 426 cm^{-1} in the region of iodate deformations. The expected frequency position of the remaining A-modes is listed in Table S2 (ESI).

The consideration of the long-range electrostatic interactions splits the infrared polar modes (B_1, B_2 and B_3) into transverse
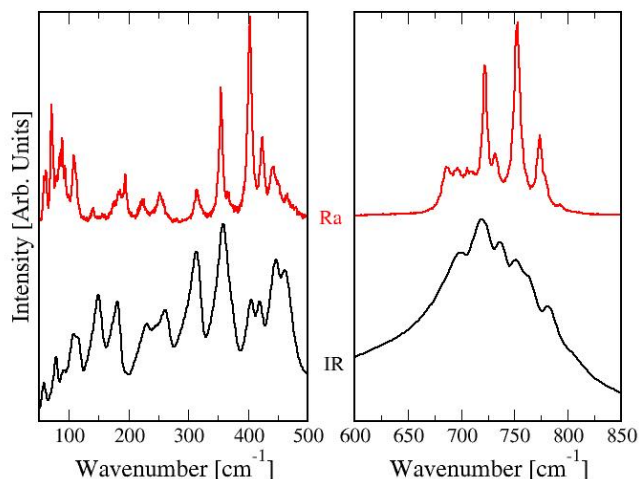
Fig. 7 Experimental infrared (IR) absorbance and Raman (Ra) spectra of CDI recorded at room temperature.

optical (TO) and longitudinal optical (LO) components close to the Γ-point. The LO–TO splitting can be computed from the knowledge of the Born effective charges and the electronic dielectric tensor[52]. Mathematically, a non-analytical contribution is added to the analytical contribution of the dynamical matrix and the full dynamical matrix (analytical + non-analytical) is re-diagonalized. The splitting of the B_1, B_2 and B_3 modes can be observed when the electric field is along the c, b and a crystal directions, respectively. The strength of the LO-TO splitting can be estimated from infrared reflectivity (Figure 8). Reflectivity spectra have been computed at normal incidence according to the methodology from ref.[52]. As the damping of modes has not been considered, the calculated reflectivities saturate to the unity. Figure 8 shows that the LO-TO splitting is small (<5 cm^{-1}) for lattice modes (below 300 cm^{-1}) and it becomes bigger and bigger going from the region of iodate deformations to that of stretching vibrations. This splitting reaches a maximal value of 55 cm^{-1} for the B2 TO mode at 560 cm^{-1}.

### 4.4 Piezoelectric response

The CDI piezoelectric-stress has three independent elements, namely e_{41}, e_{52} and e_{63}. No other non-zero element can be found by symmetry. These three elements respectively describes the induced polarization along the x-, y- or z-direction when a shear strain is applied in the orthogonal plane to the polarization. To date, the CDI piezoelectric response has never been measured nor calculated. Table 3 lists the calculated values of the three piezoelectric constants in the zero Kelvin limit. We observe that they share the same sign. The nature of the sign (here negative) is not meaningful as these three elements could be have the same positive sign by reversing the axis directions. The piezoelectric response along y-direction is the smallest with e_{52} =-0.05 C/m^2. The response for the two other directions is much bigger: e_{41} =-

Calc. [cm^{-1}]		Expmt. [cm^{-1}]			Calc. [cm^{-1}]		Expmt. [cm^{-1}]		
Sym.	PBEvdW [0 K]	Infrared [35 K]	Infrared [295 K]	Raman [295 K]	Sym.	PBEvdW [0 K]	Infrared [35 K]	Infrared [295 K]	Raman [295 K]
B_2	41		39		B_3	327	351	346	349
B_1	59	61	59	59	B_1,B_2	333–337	361	358	355
B_3	63	64	62	62	B_1, B_2	351–355	377	371	366
B_1	77	76	72	72	B_1	383	409	404	403
B_3	79	81	79	79	B_2	401	425	420	420
B_1	84	84	81	83	B_3	408		424	424
B_1	90			85	A	416			426
B_2	93	95	91	89	B_1	420	450	446	443
B_3	95			94	A	430			450
B_3	104	107	102	100	B_1, B_2, B_3	427–436	467	463	463
B_1	109	112	108	109	B_2, B_3	443–450	482	477	
B_2, B_3	115	118	116	114					687
B_1	130	144	139	140	B_2	560	692	699	696
B_1	142	155	149		A	577			705
B_1, B_2, B_3	152–153	160	156	157	B_1, B_3	593–598	717	720	722
B_1, B_3	170–171	177	173	173	A	623			732
B_1, B_2	185–186	189	181	183	B_2	626–630	736	738	
B_3	193	193	187	185	B_1,B_2	641-643	753	756	753
B_3	200	204	197	194			764	765	
B_1,B_2,B_3	220	226	218	220	B_1	674	782	782	779
B_3	237	237	230	230	B_3	698	803	806	
B_1, B_2	251–254	252	246	252	A	701			774
B_1, B_2, B_3	262–265	270	261	260	B_2	707	813		
B_1, B_2	283–290	316	313	313	B_2	720			793
B_3	298	323	321	321					

Table 2 Assignment of the experimental infrared (35 and 295 K) and Raman (298 K) frequencies with the calculated ones (0 K). We considered that a Raman mode and an infrared mode are the same if their frequency difference at room temperature is below 4 cm^{-1} taking into account our experimental resolution.
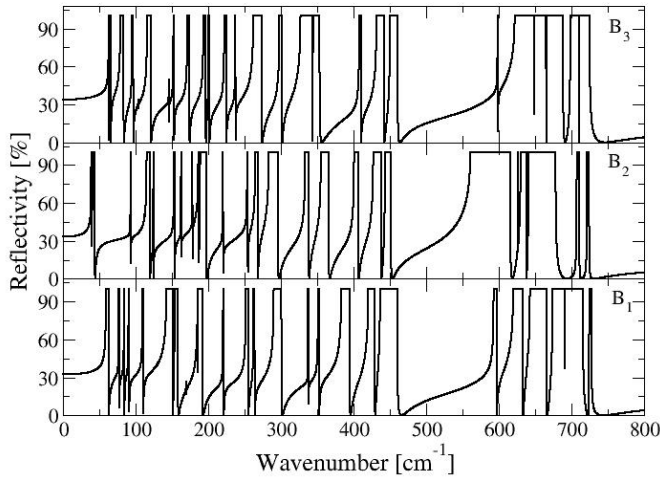
Fig. 8 Polarized reflectivity infrared spectrum of CDI calculated using the PBEvdW model. The B_1, B_2 and B_3 modes are polarized along the c, b and a crystal directions, respectively.

Index	Electronic (e^{el})	Vibrational (e^{ph})	Total ($e = e^{el} + e^{ph}$)
41	0.091	-0.358	-0.267
52	-0.003	-0.048	-0.051
63	-0.094	-0.084	-0.178

Table 3 Calculated contributions (electronic and vibrational) to the piezoelectric-stress constants in CDI. Values are given in C/m^2.

B_3-modes Freq.	e_{41}^{ph}	B_2-modes Freq.	e_{52}^{ph}	B_1-modes Freq.	e_{63}^{ph}
63	-0.053	39	0.063	59	0.109
65	-0.028	41	-0.041	77	0.032
79	-0.051	93	-0.043	84	0.025
95	0.053	112	0.007	90	-0.016
104	0.001	115	-0.003	109	-0.004
116	-0.017	125	0.003	130	0.001
146	-0.012	153	0.047	142	-0.062
152	-0.044	163	-0.029	154	-0.036
171	-0.059	178	0.022	170	-0.009
193	-0.090	186	-0.073	185	-0.035
200	-0.048	189	0.040	185	0.016
222	0.004	220	0.019	220	-0.017
237	0.007	254	0.021	252	0.007
262	0.048	265	0.028	262	0.009
298	-0.006	283	0.064	290	-0.095
327	0.054	333	0.019	337	-0.002
344	-0.002	355	-0.032	351	-0.001
408	-0.035	401	-0.104	383	-0.041
431	0.039	427	0.052	420	0.094
450	0.013	443	0.020	436	0.044
598	-0.066	561	0.080	593	0.190
622	-0.028	626	-0.001	619	-0.096
649	-0.010	630	-0.165	643	-0.157
666	0.010	641	-0.062	674	-0.036
698	-0.045	707	0.027	691	-0.009
711	0.005	721	-0.002	724	0.003
Iodate stretching modes (500–800 cm^{-1})					
Total	-0.134		-0.123		-0.105
Iodate deformation modes (270–500 cm^{-1})					
Total	+0.063		+0.019		-0.001
Lattice modes (<270 cm^{-1})					
Total	-0.289		+0.061		+0.020

Table 4 Contributions of the vibrational polar normal modes to the vibrational piezoelectric-stress (in C/m^2) in CDI. Frequencies are reported in cm^{-1}.

0.27 C/m^2 and e_{63} =-0.18 C/m^2. These values cannot be rigorously compared among the $M^{II}(IO_3)_2$ family as only CDI belongs to the $P2_12_12_1$ space group. A similar value about 0.2 C/m^2 is predicted for e_{41} in α-quartz-type $GaAsO_4$ [27]. However, this value is much smaller than that reported in other iodates like α-LiO$_3$ with hexagonal structure [12].

To have a deeper insight, we have identified the electronic (e^{el}) and the phonon-mediated (e^{ph}) contributions for each elements of the piezoelectric-stress tensor (Table 3). The electronic contribution to e_{52} is almost zero. The origin of the e_{52} value is therefore purely associated to the phonon dynamics of B_2-modes. The electronic contribution to e_{41} and e_{63} is the same in absolute value (about 0.09 C/m^2), but has an opposite sign. This indicates that a shear strain of the unit cell in the (xy)-plane (resp. (yz)-plane) will yield to a reduction (resp. an increase) of the electronic polarization along the z-direction (resp. x-direction).

The phonon-mediated contribution has a different behaviour for e_{41} and e_{63}. For e_{63}, the vibrational and the electronic contributions have similar magnitude and share the same negative sign. This situation is the most favorable because there is no possible reduction of the piezoelectric response either from the electrons or the phonons. Nevertheless, the small value of these two contributions ($\sim$-0.09 C/m^2) does not yield to a very high value of

the overall e_{63} (-0.18 C/m^2). In the case of e_{41}, the situation is less favorable as the vibrational and the electronic contributions have an opposite sign. The electronic contribution decreases the dominant vibrational contribution, yielding to e_{41} =-0.27 C/m^2.

The participation of the normal modes to the vibrational contribution can be calculated as [53]:

$$e_{j\alpha}^{ph}(m) = \frac{1}{\Omega_0} \frac{1}{\omega_m^2} \sum_{\beta,\kappa} Z_{\alpha\beta}^*(\kappa) U_\beta(\kappa,m) \sum_{\gamma,\kappa'} \Lambda_\gamma^j(\kappa') U_\gamma(\kappa',m) \qquad (3)$$

where (α,β,γ) stands for the cartesian directions and (κ,κ') labels the atoms in the unit cell. In this equation, Ω_0 is the unit cell volume, Z^* is the Born effective charge, $U(m)$ is the mth eigendisplacement vector with frequency ω_m and Λ is the force-response internal-strain coupling. Thus, $e_{j\alpha}^{ph}$ is sizable for a low frequency mode combining high infrared intensity (the first sum in Eq. (3) is the mode polarity which is linked to the mode oscillator strength) and strong coupling with strain (second sum in Eq. (3)). Contributions of each zone-center normal mode are listed in Table 4.

Only the normal modes belonging to the B$_3$-, B$_2$- or B$_1$-representation contribute to e_{41}^{ph}, e_{52}^{ph} or e_{63}^{ph}, respectively. Modes belonging to the A-representation are not involved in the piezoelectric effect as they are non polar. For e_{41}^{ph}, the external modes (below 270 cm^{-1}) and the stretching of the iodate groups strongly contribute to the vibrational contribution because they bring about -0.42 C/m^2. In contrast, the deformation of the iodate groups decreases the vibrational contribution by +0.06 C/m^2. Among the external lattice modes, we do not have dominant modes. Each mode has a positive or negative participation. In contrast, all stretching modes contribute to increase e_{41}^{ph} except the modes centered at 666 and 711 cm^{-1}. The contribution of these modes are important despite their quite high frequencies. Among the deformation of the iodate groups, the B$_3$-modes centered at 327, 408 and 431 cm^{-1} give the highest contributions. In the case of e_{52}^{ph}, the stretchings of the iodate groups bring -0.12 C/m^2 which is counterbalanced by the B$_2$-modes with frequencies below 500 cm^{-1}, yielding to the smallest vibrational contribution in CDI (e_{52}^{ph} =-0.05 C/m^2). The B$_2$-modes centered at 401, 561 and 630 cm^{-1} give the highest contribution. The contribution of the iodate deformations to e_{63}^{ph} is almost zero. The stretchings of iodate groups (-0.11 C/m^2) dominate e_{63}^{ph} despite a very small compensation of the external modes below 270 cm^{-1}. The B$_1$-modes centered at 59, 290, 420, 593, 619 and 643 cm^{-1} give the highest contribution.

Note that $e_{j\alpha}^{ph}$ could be overestimated in our calculations (without an eventual error compensation) because of the position of the iodate stretching bands at much smaller frequencies than in the experiment. To estimate this overestimation, we shifted the frequencies associated with the stretching of iodates by 100 cm^{-1} to have a better agreement with the experimental frequencies and re-calculated $e_{j\alpha}^{ph}$. As expected, the vibrational contribution is smaller with this shift and we get: e_{41}^{ph} =-0.33, e_{52}^{ph} =-0.02 and e_{63}^{ph} =-0.06 C/m^2. Thus, this small difference with the values reported in Table 3 suggests that our calculations should give reliable predictions on the magnitude of the piezoelectric-stress constants despite the poor agreement calculation/experiment on the position of the iodate stretchings. In the case of α-LiIO$_3$, a quite good agreement is obtained between the experimental piezoelectric constants and the calculated[12,47] ones despite the similar strong underestimation in the calculation of the iodate stretching vibrations (500–900 cm^{-1}).

The phonon-mediated contribution can also be analyzed from the polyhedron representation as building block of the CDI structure (Figure 3). According to x-ray studies, the CDI structure has three independent polyhedra labelled P(Cd), P(I1) and P(I2) (see section IV.A.). The contribution of each independent polyhedron to e^{ph} has been estimated as[53,54]:

$$e_{j\alpha}^{ph}[P(i)] = Z \left[e_{j\alpha}^{ph}(i) + \frac{1}{f} \sum_{O \in P_i} e_{j\alpha}^{ph}(O) \right], \quad (4)$$

where i ={Cd, I1, I2}, Z is the number of formula units (Z =4) and f is an integer number given the number of polyhedra sharing the same oxygen atom. This number is equal to 2 for all oxygen except the three oxygens sharing two CdO$_7$ polyhedra where

Polyhedron	e_{41}^{ph}	e_{52}^{ph}	e_{63}^{ph}
P(Cd)	-0.218	-0.172	-0.069
P(I1)	-0.202	0.008	-0.163
P(I2)	0.059	0.119	0.146

Table 5 Calculated vibrational contribution (e^{ph}) of each polyhedron P(X) to the overall piezoelectric-stress (e) in CDI. Only independent elements are listed and their values are given in C/m^2. P(X) is the polyhedron centered on the X-atom (see text).

Index	$C^{(\mathscr{E})}$ (GPa)	$S^{(\mathscr{E})}$ (TPa^{-1})
11	60.61	25.61
22	63.97	21.13
33	65.95	21.43
44	25.91	38.59
55	28.22	35.43
12	29.92	-8.20
13	32.51	-9.44
23	25.59	-4.16

Table 6 Calculated elastic ($C^{(\mathscr{E})}$) and compliance ($S^{(\mathscr{E})} = [C^{(\mathscr{E})}]^{-1}$) constants defined under the condition of fixed (vanishing) electric field in CDI.

f =3. The atom-contribution, $e_{j\alpha}^{ph}(\kappa)$, of a κ-atom in the unit cell is given by[53,54]:

$$e_{j\alpha}^{ph}(\kappa) = \frac{1}{\Omega_0} \sum_\beta Z_{\alpha\beta}^*(\kappa) \frac{du_\beta(\kappa)}{d\eta_j} \quad (5)$$

where $du/d\eta$ is the displacement-response internal-strain that describes the first-order displacements resulting from a first-order strain. Results of this projection are shown in Table 5. The P(Cd) and P(I1) polyhedra equaly contribute to e_{41}^{ph} and bring together $\sim$-0.21 C/m^2. These contributions are slightly decreased by the P(I2) polyhedra. The contribution of the P(Cd) polyhedra to e_{52}^{ph} is dominant, but almost counterbalanced by the polyhedra centered on iodine atoms. In the case of e_{63}^{ph}, the situation is similar to that with e_{41}^{ph}, but the compensation by the P(I2) polyhedra is stronger. Thus, the P(I2) polyhedra lead in all cases to a decrease in the vibrational piezoelectric response.

There are three sets of piezoelectric tensors, labelled d, g and h. Each of them is more suited to a particular property. For instance, the piezoelectric-strain tensor[54],

$$d_{j\alpha} = \sum_k S_{jk}^{(\mathscr{E})} e_{k\alpha} \quad (6)$$

where $S^{(\mathscr{E})}$ is the elastic compliance tensor defined under the condition of fixed (vanishing) electric field, estimates the magnitude of the piezoelectric response in an actuator. The full elastic tensor in CDI has eight independent elastic constants: $C_{11}^{(\mathscr{E})}$, $C_{22}^{(\mathscr{E})}$, $C_{33}^{(\mathscr{E})}$, $C_{44}^{(\mathscr{E})}$, $C_{55}^{(\mathscr{E})}$, $C_{12}^{(\mathscr{E})}$, $C_{13}^{(\mathscr{E})}$ and $C_{23}^{(\mathscr{E})}$. These constants are listed in Table 6 and satisfy the Born stability inequalities[55] for the orthorhombic space group, which indicates that this structure is mechanically stable. Some important elastic properties can be calculated

from the knowledge of these constants as: the bulk (B) and shear (G) moduli and the shear anisotropy factor (A). The bulk and shear moduli computed from the Voigt-Reuss-Hill approximation are: $B = 20.38$ GPa and $G = 5.99$ GPa. Their ratio of 3.40 indicates a ductile character according to Push's criteria[56] ($B/G > 1.75$). The shear anisotropy factors for the {100}-, {010}- and {001}-planes are 1.68, 1.43 and 1.38, respectively. These values close to the unity suggest that the shear anisotropy in CDI crystal is relatively small. The strongest anisotropy could be observed for the {100}-plane (between the [010] and [001] direction). At zero pressure, the small violation of the Cauchy criterion[57] (-0.3, +4.3 and +7.5 GPa for the {100}-, {010}- and {001}-plane, respectively) indicates a strong ionic character of bonds in CDI.

In CDI, Eq. (6) is strongly simplified and the sum is reduced to only one term: $d_{j\alpha} = e_{j\alpha} S_{jj}^{(\mathscr{E})}$. As a consequence, the $d_{j\alpha}/e_{j\alpha}$ ratio is directly equal to the elastic compliance $S_{jj}^{(\mathscr{E})}$ and does not depend on other terms. The values of $S_{44}^{(\mathscr{E})}$, $S_{55}^{(\mathscr{E})}$ and $S_{66}^{(\mathscr{E})}$ are positive and have a similar magnitude (~ 0.04 GPa^{-1}). Thus, the three independent piezoelectric-strain elements are arranged in the same relative order (in absolute value) than their associated piezoelectric-stress values: $d_{41} > d_{63} > d_{52}$. The highest value, $d_{41} = -10$ pC/N, is associated to the strongest shear anisotropy. This value is about two to three times higher than that reported in α-LiIO$_3$ ($3.9 < d_{41} < 5.6$ pC/N), but is considerably smaller than its highest shear value ($d_{42} = 50$ pC/N) [12,58]. The value of the d_{41} in CDI is also much higher than that reported in α-quartz-type compounds like α-SiO$_2$ ($d_{41} \sim 0.67$ pC/N) [59] or α-GaPO$_4$ ($d_{41} = 1.9$ pC/N) [60]. Large piezoelectric-strain constants is associated to large mechanical displacements which are usually sought in motional transducer devices. Conversely, these constants can be viewed as relating the charge collected on the electrodes when a mechanical stress is applied.

The electromechanical coupling factor, k, is an indicator of the efficiency of a material in converting an electrical energy into a mechanical energy or vice versa. This coupling factor is defined for each mode of vibration, depending on the direction of polarization and the shape of the sample (plate, bar or disk). In the case of CDI, k describes the energy conversion in a thickness shear vibration and it has been calculated according to:

$$k_{j\alpha}^2 = \frac{e_{j\alpha}^2}{\varepsilon_{\alpha\alpha}^{(\eta)} \varepsilon_0 C_{jj}^{(\mathscr{E})} + e_{j\alpha}^2}, \tag{7}$$

where $\varepsilon^{(\eta)}$ is the fixed-strain dielectric constant and ε_0 is the vacuum permittivity. To have the most reliable prediction on k, $\varepsilon^{(\eta)}$ has been scissors-corrected in this calculation (see next section). Shear coupling coefficients are usually measured using the thickness-shear resonance following the IEEE standards[61]. They have practical importance for making shear transducers for example. The best electromechanical conversion in CDI is observed for k_{41} with an efficiency about 15% (Table 7). Thus, CDI provides higher electromechanical coupling than α-LiIO$_3$ ($5 < k_{41} < 7$ %) [58] and similar coupling with a rotated shear vibration (AT-cut) of α-GaPO$_4$ ($k_{26} = 16$%) [62]. In the case of a shear mode piezoelectric resonator application, the use of a X-cut will give the best

Index	d [pC/N]	k [%]	g [m^2/C]	h [GN/C]
41	-10.323	15.0	-0.080	-7.976
52	-1.697	2.6	-0.014	-0.067
63	-7.976	11.3	-0.390	-1.526

Table 7 Calculated independent elements of the piezoelectric-strain (d), piezoelectric-voltage (g) and piezoelectric-stiffness (h) tensors in CDI. The electromechanical coupling factor (k) is also listed and calculated using the electronic dielectric constant, ε^∞, including the scissors correction.

piezoelectric efficiency for CDI. The values of the independent elements of the piezoelectric-voltage (g) and the piezoelectric-stiffness (h) tensors are given in Table 7 for information.

4.5 Dielectric constants

In a non-magnetic acentric material, the free-stress dielectric constant, $\varepsilon^{(\sigma)}$, can be decomposed as the sum of three contributions (neglecting crossed terms):

$$\varepsilon_{\alpha\beta}^{(\sigma)} = \varepsilon_{\alpha\beta}^\infty + \varepsilon_{\alpha\beta}^{ph} + \varepsilon_{\alpha\beta}^{piezo}. \tag{8}$$

The optical dielectric tensor, ε^∞, is the purely electronic response when a static field is applied. The value of this contribution is usually overestimated when compared to the experimental ones. This problem is also linked to the underestimation of the electronic band gap in common exchange–correlation functional (see Sec. 4.2). We used a scissors operator[22] to fix this problem. This consists in an empirical rigid shift of the conduction bands to adjust the GGA band gap to the experimental value. By comparing our calculated band gap value ($E_g^{calc} = 2.85$ eV) with the experimental one ($E_g^{exp} = 4.6$ eV), the scissors correction is fixed to 1.75 eV. As expected, this correction leads to a decrease in the values of the optical dielectric tensor (see Table 8). This decrease is about 17% for the three diagonal elements and does not change the small anisotropy of the tensor nor the trend ($\varepsilon_{11}^\infty > \varepsilon_{22}^\infty > \varepsilon_{33}^\infty$). The refractive optical index after the scissors correction is estimated to be: [2.04, 2.02, 1.99]. The second contribution in Eq. (8) is the phonon-mediated response to the electric field and is a function of the infrared oscillator strength, A. This contribution is listed in Table 8 and has been calculated according to a system of undamped harmonic oscillators (in cgs units) [53]:

$$\varepsilon_{\alpha\beta}^{ph} = \frac{4\pi}{\Omega_0} \sum_m \frac{A_{\alpha\beta}(m)}{\omega_m^2} \tag{9}$$

where the sum runs over all polar modes. This phonon-mediated response is the dominant contribution to $\varepsilon^{(\sigma)}$ and increases the dielectric constant to a mean value about 13, including or not the scissors correction. The mode-by-mode decomposition (not reported) shows that there is no clear dominant phonon mode whatever the direction and therefore all phonons contribute to ε^{ph}.

The third and last contribution in Eq. (8) is the response of the strain to the electric field and is a function of the piezoelectric-stress constant, e. This contribution, listed in Table 8, is defined

Table 8 Electronic, vibrational and piezoelectric contributions to the dielectric tensor in CDI. Values with scissors correction fixed to 1.75 eV are between brackets.

Index ->	11	22	33
Electronic (ε^∞)	4.982	4.921	4.731
	(4.146)	(4.089)	(3.979)
Vibrational (ε^{ph})	9.273	8.957	8.467
Piezoelectric (ε^{piezo})	0.312	0.009	0.161
Total	14.567	13.887	13.359
	(13.731)	(13.055)	(12.607)

by[54]:

$$\varepsilon^{piezo}_{\alpha\beta} = \sum_{j,k} e_{\alpha j} S^{(\mathscr{E})}_{jk} e_{k\beta}. \tag{10}$$

We observe that the strain relaxation has a small influence on the overall values of the dielectric constant whatever the direction. The highest variation ($\sim 2\%$ of the overall value) is observed along the x-direction as the e_{41} piezoelectric-stress constant has the highest value (Table 3). For the two other cartesian directions, the contribution of the strain relaxation is negligible. In practice, $\varepsilon^{(\sigma)}$ should be compared to ac dielectric measurements at frequencies much less than sample resonances.

5 Conclusions

The δ-phase of cadmium diiodate has been synthesized by evaporation and tiny single crystals have been collected. The x-ray diffraction showed an orthorhombic $P2_12_12_1$ space group in agreement with the literature. This compound stays thermally stable until 550°C. We demonstrated that the van der Waals correction to the PBE exchange–correlation functional improves the calculation of the CDI crystallographic structure with respect to other kinds of functionals. We revisited the nature of the electronic band gap from UV-vis spectroscopy and suggest an indirect band gap with a value of 4.6 eV. This result is consistent with our electronic band structure calculations. The infrared and Raman responses were measured and the different phonon modes assigned with the support of DFPT-based calculations.

The three independent piezoelectric-stress constants (e_{41}, e_{52} and e_{63}) have been calculated and we discussed their origin by the analysis of their electronic and the vibrational contributions. We found that the phonon-mediated contribution is the dominant contribution for e_{41} and e_{52}. In contrast, there is no dominant contribution for e_{63}. The vibrational contribution has been also analyzed using two complementary approaches: the normal modes of vibration and the different polyhedra used as building block of the CDI structure. The external lattice modes (below 270 cm^{-1}) and the stretching of the iodate groups strongly contribute to e^{ph}_{41}. For e^{ph}_{52}, the stretching of the iodate groups (above 500–800 cm^{-1}) is counterbalanced by the other modes below 500 cm^{-1}, yielding the smallest vibrational contribution. The stretchings of iodate groups dominate e^{ph}_{63} and their deformations is almost zero. The polyhedral representation analysis showed that the P(I2) polyhedra lead in all cases to a decrease in the vibrational piezoelectric response.

The elastic compliance tensors and dielectric constants have been calculated and we derived the different piezoelectric tensors (e, d, g, h and k) in CDI. For example, the highest value of the piezoelectric-strain in the zero Kelvin limit is predicted for $d_{41} = -10.32$ pC/N. This sizable value associated with the thermal stability (no phase transition up to its thermal decomposition at 550 °C) and a relative large electronic band gap make δ-Cd(IO$_3$)$_2$ a potential candidate for piezoelectric applications.

Conflicts of interest

There are no conflicts to declare.

Notes and references

1 C.-L. Hu and J.-G. Mao. Recent Advances on Second-Order NLO Materials on Metal Iodates. *Coord. Chem. Rev.*, 2015, **288**, 1-17.

2 D. Phanon and I. Gautier-Luneau. Promising Material for Infrared Non-Linear Optics: NaI$_3$O$_8$ Salt Containing an Octaoxotriiodate(V) Anion Formed From Condensation of [IO$_3$]$^-$ Ions. *Angew. Chem.*, 2007, **46**, 8488-8491.

3 K. M. Ok and P. S. Halasyamani. The Lone-Pair I(5$^+$) in a Hexagonal Tungten Oxide-Like Framework: Synthesis, Structure and Second-Harmonic Generating Properties of Cs$_2$I$_4$O$_{11}$. *Angew. Chem.*, 2004, **43**, 5489-5491.

4 D. Phanon and I. Gautier-Luneau. New Materials for Infrared Non-Linear Optics. Syntheses, Structural Characterisations, Second Harmonic Generation and Optical Transparency of M(IO$_3$)$_3$ Metallic Iodates. *J. Mater. Chem.*, 2007, **17**, 1123-1130.

5 C. T. Chen and G. Liu. Recent Advances in Nonlinear Optical and Electro-Optical Materials. *Rev. Mater. Sci.*, 1986, **16**, 203-243.

6 K. M. Ok, E. O. Chi and P. S. Halasyamani. Bulk Characterization Methods for Non-Centrosymmetric Materials: Second-Harmonic Generation, Piezoelectricity, Pyroelectricity, and Ferroe lectricity. *Chem. Soc. Rev.*, 2006, **35**, 710-717.

7 C. Wang, T. Zhang and W. Lin. Rational Synthesis of Noncentrosymmetric Metal-Organic Frameworks for Second-Order Nonlinear Optics *Chem. Rev.*, 2012, **112**, 1084-1104.

8 W. Zhang and R.-G. Xiong. Ferroelectric Metal-Organic Frameworks *Chem. Rev.*, 2012, bf 112, 1163-1195.

9 K. M. Ok and P. S. Halasyamani. New Selenites: Syntheses, Structures, and Characterization of Centrosymmetric Al$_2$(Se$_2$O$_5$)$_3$ and Ga$_2$(Se$_2$O$_5$)$_3$ and Non-centrosymmetric In$_2$(Se$_2$O$_5$)$_3$ *Chem. Mater.*, 2002, **14**, 2360-2364.

10 C. F. Sun, B. P. Yang and J. G. Mao. Structures and Properties of Functional Metal Iodates. *Sci. China. Chem.*, 2011, **54**, 911-922.

11 S. Haussühl. Piezoelektrisches und Elektrisches Verhalten von Lithiumjodat. *Phys. Stat. Sol. (b)*, 1968, **29**, K159-K162.

12 P. Hermet. First-Principles Based Analysis of the Piezoelectric Response in α-LiIO$_3$. *Comput. Mater. Sci.*, 2017, **138**, 199-203.

13 S. C. Abrahams, R. C. Sherwood, J. L. Bernstein and K. Nassau. Transition Metal Iodates: Crystallographic, Magnetic

and Nonlinear Optic Survey of the 3d Iodates. *J. Solid State Chem.*, 1973, **7**, 205-212.

14 S. C. Abrahams, R. C. Sherwood and J. L. Bernstein. Crystal Structure and Pyroelectric Coefficient of $Co(IO_3)_2$ and Non-Centrosymmetric 3d-Transition Metal Iodates. *J. solid state Chem.*, 1981, **36**, 195-204.

15 X. Chen, W. Xiao, X. Chang and H. Zang. Hydrothermal Synthesis and Crystal Structure of Strontium Iodate, $Sr(IO_3)_2$. *J. Alloys and Compounds*, 2004, **381**, 229-233.

16 G. J. Shanmuga Sundar, S. M. Ravi Kumar, M. Packiya Raj and S. Selvakumar. Synthesis, Growth, Optical, Mechanical and Dielectric Studies on NLO Active Monometallic Zinc Iodate $[Zn(IO_3)_2]$ Crystal for Frequency Conversion. *Mater. Res. Bul.*, 2019, **112**, 22-27.

17 D. Phanon, B. Bentria, E. Jeanneau, D. Benbertal, A. Mosset and I. Gautier-Luneau. Crystal Structure of $M(IO_3)_2$ Metal Iodates, Twinned by Pseudo-Merohedry, with M^{II}: Mg^{II}, Mn^{II}, Co^{II}, Ni^{II} and Zn^{II}. *Z. Kristallogr.*, 2006, **221**, 635-642.

18 Y.-J. Jia, Y.-G. Chen, Y. Gao, X.-F. Guan, C. Li, B. Li, M.-M. Liu and X.-M. Zhang. $LiM^{II}(IO_3)_3$ (M^{II} = Zn and Cd): Two Promising Nonlinear Optical Crystals Derived From a Tunable Structure Model of α-$LiIO_3$, *Angew. Chem.*, 2019, **58**, 17194-17198.

19 B.-P. Yang and J.-G. Mao. Synthesis, Crystal Structure and Optical Properties of Two Layered Cadmium Iodates: $Cd(IO_3)X$ (X= Cl, OH). *J. Solid State Chem.*, 2014, **219** 185-190.

20 S. L. Garud and K. B. Saraf. Growth and Study of Mixed Crystals of Ca-Cd Iodate. *Bull. Mater. Sci.*, 2008, **31**, 639-643.

21 B. Bentria, D. Benbertal, Z. Hebboul, M. Bagieu-Beucher and A. Mosset. Polymorphism of Anhydrous Cadmium Iodate, Structure of ε-$Cd(IO_3)_2$. *Z. Anorg. Allg. Chem*, 2005, **623**, 894-901.

22 H. Bach. Dissertation Univsersität Köln (1976).

23 H. Bach and H. Küppers. Cadmium Diiodate. *Acta Cryst. B*, 1978, **34**, 263-265.

24 S. M. Ravi Kumar, N. Melikechi, S. Selvakumar and P. Sagayaraj. Crystal Growth and Characterization of Monometallic NLO Single Crystals of $Cd(IO_3)_2$. *J. Cryst. Growth*, 2009, **311**, 337-341.

25 S. J. Shitole. Study of XRD, FTIR, Thermal Analysis and Nonlinear Optical Properties of Barium, Calcium, Cadmium Iodate Crystals Grown in Silica Hydro Gel. *IJCA Proceedings on National Conference on Advances in Communication and Computing*, 2014, **2**, 23-29.

26 Z. Hebboul and D. Benbertal. Synthesis and Characterization of New Anhydrous Cadmium Iodate Zeta Polymorph ζ-$Cd(IO_3)_2$. *J. Mater. Environ. Sci.*, 2018, **9**, 565-569.

27 P. Hermet, J. Haines, J.-P. Aubry and O. Cambon. Origin and Mechanism of Piezoelectricity in α-Quartz-type $M^{III}X^VO_4$ Compounds (M = B, Al, or Ga; X = P or As). *J. Phys. Chem. C*, 2016, **120**, 26645-26651.

28 M. Souleiman, P. Hermet, A. Haidoux, C. Levelut, J. Haines and O. Cambon. Combined Experimental and Theoreti-cal Raman Scattering Studies of α-Quartz-Type $FePO_4$ and $GaPO_4$ End Members and $Ga_{1-x}Fe_xPO_4$ Solid Solutions. *RSC Advances*, 2013, **3**, 22078.

29 D. Clavier, M. Prakasam, A. Largeteau, J. J. Boy, B. Hehlen, M. Cambon, P. Hermet, J. Haines and O. Cambon. Piezoelectric and Non-Linear Optical Properties of α-Quartz Type $Si_{1-x}Ge_xO_2$ Single Crystals. *Cryst. Eng. Comm.*, 2016, **18**, 2500-2508.

30 D. Clavier, P. Hermet, A. Van der Lee, J. Haines and O. Cambon. Prediction of Piezoelectric Properties by First Principles Calculations and Hydrothermal Crystal Growth of $Si_{1-x}Sn_xO_2$ α-Quartz Phase. *Cryst. Eng. Comm.*, 2018, **20**, 7479-7485.

31 X. Gonze, B. Amadon, P. M. Anglade, J. M. Beuken, F. Bottin, P. Boulanger, F. Bruneval, D. Caliste, R. Caracas, *et al.* ABINIT: First-principles Approach to Material and Nanosystem Properties. *Comput. Phys. Comm.*, 2009, **180**, 2582-2615.

32 J. P. Perdew, K. Burke and M. Ernzerhof. Generalized Gradient Approximation Made Simple. *Phys. Rev. Lett.*, 1996, **77**, 3865-3868.

33 A. D. Becke and E. R. Johnson. A Simple Effective Potential for Exchange. *J. Chem. Phys.*, 2006, **124**, 221101.

34 S. Grimme, S. Ehrlich and L. Goerigk. Effect of the Damping Function in Dispersion Corrected Density Functional Theory. *J. Comput. Chem.*, 2011, **32**, 1456-1465.

35 H. J. Monkhorst and J. D. Pack. Special Points for Brillouin-Zone Integrations. *Phys. Rev. B*, 1976, **13**, 5188-5192.

36 G. Kresse, J. Furthmüller. Efficient Iterative Schemes for Ab Initio Total-Energy Calculations Using a Plane-Wave Basis Set. *Phys. Rev. B*, 1996, **54**, 11169-11185.

37 G. Bergerhoff, M. Berndt, K. Brandenburg and T. Degen. Concerning Inorganic Crystal Structure Types. *Acta Cryst. B*, 1999, **55**, 147-156.

38 $\Delta = 0$ when two structures are identical.

39 J. P. Perdew, A. Ruzsinszky, G. I. Csonka, O. A. Vydrov, G. E. Scuseria, L. A. Constantin, X. Zhou and K. Burke. Restoring the Density-Gradient Expansion for Exchange in Solids and Surfaces. *Phys. Rev. Lett.*, 2008, **100**, 136406.

40 J. P. Perdew and Y. Wang. Accurate and Simple Analytic Representation of the Electron-gas Correlation Energy. *Phys. Rev. B*, 1992, **45**, 13244-13249.

41 J. Tauc, R. Grigorivici and A. Vancu. Optical Properties and Electronic Structure of Amorphous Germanium. *Phys. Stat. Sol.*, 1966, **15**, 627-637.

42 J. P. Perdew. Density Functional Theory and the Band Gap Problem. *Int. J. Quantum Chem.*, 1985, **28**, 497-523.

43 J. Sun, A. Ruzsinszky and J. P. Perdew. Strongly Constrained and Appropriately Normed Semilocal Density Functional. *Phys. Rev. Lett.*, 2015, **115**, 036402.

44 F. Tran and P. Blaha. Accurate Band Gaps of Semiconductors and Insulators with a Semilocal Exchange-Correlation Potential. *Phys. Rev. Lett.*, 2009, **102**, 226401.

45 R. Leparc, V. T. Freitas, P. Hermet, A. M. Cojocariu, X. Cat-

toën, H. Wadepohl, D. Maurin, C. H. Tse, J. R. Bartlett, R. A. S. Ferreira, L. D. Carlos, M. Wong Chi Man and J.L. Bantignies. Infrared and Raman spectroscopy of Non-conventional Hydrogen Bonding Between N,N'-Disubstituted Urea and Thiourea Groups: a Combined Experimental and Theoretical Investigation. *Phys. Chem. Chem. Phys*, 2019, **21**, 3310-3317.

46 P. Hermet, J.-L. Bantignies, A. Rahmani, J.-L. Sauvajol, M. R. Johnson and F. Serein. Far- and Mid-Infrared of Crystalline 2,2'-Bithiophene: Ab Initio Analysis and Comparison with Infrared Response. *J. Phys. Chem. A*, 2005, **109**, 1684-1691.

47 B. Van Troeye, Y. Gillet, S. Poncé and X. Gonze. First-Principles Characterization of the Electronic and Optical Properties of Hexagonal $LiIO_3$. *Optical Mater.*, 2014, **36**, 1494-1501.

48 A. Liang, S. Rahman, P. Rodriguez-Hernandez, A. Munoz, F. Javier Manjón, G. Nenert and D. Errandonea. High-Pressure Raman Study of $Fe(IO_3)_3$: Soft-Mode Behavior Driven by Coordination Changes of Iodine Atoms. *J. Phys. Chem. C*, 2020, **124**, 21329-21337.

49 G. Herzberg. Infrared and Raman Spectra of Polyatomic Molecules. Ed. Van Nostrand (1945).

50 W. E. Dasent and T. C. Waddington. Iodine-Oxygen Compounds. Part I . Infrared Spectra and Structure of Iodates. *J. Chem. Soc.*, 1960, 2429-2432.

51 K. Nassau, J. W. Shiever and B. E. Prescot. Transition Metal Iodates. I. Preparation and Characterization of the 3d Iodates. *J. Solid State Chem*, 1973, **7**, 186-204.

52 X. Gonze and C. Lee. Dynamical matrices, Born effective Charges, Dielectric Permittivity Tensors, and Interatomic Force Constants from Density-Functional Perturbation Theory. *Phys. Rev. B*, 1997, **55**, 10355-10368.

53 P. Hermet. Piezoelectric Response in α-Quartz-Type GeO_2. *J. Phys. Chem. C*, 2016, **120**, 126-132.

54 X. Wu, D. Vanderbilt and D. R. Hamann. Systematic Treatment of Displacements, Strains, and Electric Fields in Density-Functional Perturbation Theory. *Phys. Rev. B*, 2005, **72**, 035105.

55 H. Ozisik, K. Colakoglu, H. B. Ozisik and E. Deligoz. Structural, Elastic, and Lattice Dynamical Properties of Germanium Diiodide (GeI_2). *Comput. Mater. Sci.*, 2010, **50**, 349-355.

56 S. F. Pugh. Relations Between the Elastic Moduli and the Plastic Properties of Polycrystalline Pure Metals. *Philos. Mag.*, 1954, **45**, 823-843.

57 S. P. Singh, D. Singh, N. Singh and M. N. Shukla. Study of Elastic Properties of Prototype Solids Under High Pressure. *Comput. Condens. Matter*, 2022, **30**, e00626.

58 R. Lec and W. Soluch. The Elastic, Piezoelectric, Dielectric and Acoustic Properties of $LiIO_3$ Crystals. *IEEE Ultrasonics Symposium Proceedings*, 1977, 389-392.

59 P. H. Carr. Measurement of the Piezoelectric Constant of Quartz at Gigacycle Frequencies. *J. Acoust. Soc. Am.*, 1967, **41**, 75-83.

60 W. Wallnöfer, P. W. Krempl and A. Asenbaum. Determination of the Elastic and Photoelastic Constants of Quartz-Type $GaPO_4$ by Brillouin Scattering. *Phys. Rev. B*, 1994, **49**, 10075-10080.

61 IEEE Standard on Piezoelectricity, ANSI/IEEE Std. 176-1978, New IEEE (1978).

62 J. Nosek and M. Pustka. Determination of the Electromechanical Coupling Factor of Gallium Orthophosphate ($GaPO_4$) and its Influence on Resonance-Frequency Temperature Dependencies. *IEEE transactions, Ferroelectrics and frequency control*, 2006, **53**, 10-14.